Multiply charged topological phonons in $K_2Pb_2O_3$

Chenyang Wang, Lei Jin,* Lu Tian, Wei-Wang Yu, Xiaoming Zhang, Guodong Liu, and Ying Liu†
State Key Laboratory of Reliability and Intelligence of Electrical Equipment, Hebei University of Technology, Tianjin 300130, China and School of Materials Science and Engineering, Hebei University of Technology, Tianjin 300130, China

(Received 9 February 2024; revised 26 April 2024; accepted 29 May 2024; published 13 June 2024)

Topological phonons have attracted tremendous attention in recent years, particularly when topological phonons have nonzero topological numbers and exhibit many peculiar physical phenomena. However, studies on the coexistence of different phonons with nonzero topological charge are quite limited. Here, we reveal a realist material $K_2Pb_2O_3$, which can realize the coexistence of three types of phonons, namely charge-1 Weyl point (WP), charge-2 triple point (TP), and charge-4 WP. We perform symmetry analysis for these points, presenting symmetry conditions to realize these topological phonons, and constructing an effective model to describe them. Meanwhile, we calculate the phonon spectrum, topological surface states, and the constant frequency slice for $K_2Pb_2O_3$, and we perform the Wilson loop method to calculate the Chern number for WPs and TPs in the material. The results indicate that the material $K_2Pb_2O_3$ has charge-1 WPs, charge-2 TPs, and charge-4 WPs at high-symmetry points in the range of 13–19 THz. In particular, the phonon spectrum within this range solely contains the bands responsible for forming these topological band-crossing points. The Fermi arcs emanating from the projections of a charge-1 WP, a charge-2 TP, and a charge-4 WP are connected with each other, forming a long Fermi arc extended in the whole Brillouin zone, which greatly facilitates observation in experiment by neutron scatterings or high-resolution electron energy loss spectroscopy. Our work provides a platform for studying charge-1 WP, charge-2 TP, and charge-4 WP in a phononic system.

DOI: 10.1103/PhysRevB.109.235415

I. INTRODUCTION

The field of condensed-matter physics has witnessed a surge in interest surrounding topological materials due to their unique properties [1–6]. Exploring various fermion types has been a key aspect of this research, ranging from Dirac fermions in graphene to Majorana fermions in superconducting heterostructures [7–12]. The discovery of diverse fermions includes triple, sixfold, and eightfold fermions, as well as nodal line/ring/net structures [13–18]. Despite these advances, the study of Weyl semimetals remains a focal point, exemplifying the convergence of high-energy physics and condensed matter [5,9].

Weyl fermions characterized by Chern numbers have garnered significant attention. The Chern number, a vital topological invariant, classifies semimetallic topological nodes, especially in Weyl semimetals where unconventional fermions with Chern numbers greater than 1 have been identified [19–21]. These fermions lead to distinct physical phenomena, influencing the number of topological Fermi arc surface states and affecting phenomena such as the quantized circular photocurrent effect and chiral Landau energy levels [2,22–27]. While many materials in the electronic system exhibit nonzero topological charges, instances of materials hosting fermions with different topological charges near the Fermi level are rare. In contrast, the realm of phonon materials, not constrained by the Pauli exclusion principle, opens up the possibility of multiple phonons with different topological charges within the same system. This presents a promising avenue for exploration in the field.

Various types of topological phonons have been identified in phononic systems, including Weyl, Dirac, triple point, nodal line, and nodal surface phonons [28–31]. Among them, Weyl phonons with Chern numbers of ±1, ±2, and ±4 have been discovered in real materials, such as α-SiO_2, MSi (M = Fe, Co, Mn, Re, Ru), $K_2Mg_2O_3$, and Nb_3Al_2N [32–34]. In particular, charge-2 Weyl phonons are observed in experiment [35]. In addition to Weyl phonons, triple-point phonons have also been proposed to exist in realistic materials, e.g., triply degenerate phonons in TaSb, charge-2 triple point in Ca_3I_3P, quadratic contact triple point in Ta_3Sn and CsTe [36–39]. Moreover, the relevant studies have shown that the presence of triple-point phonons can enhance thermoelectric response [36]. Systematic studies have explored Dirac phonons characterized by Chern numbers equal to ±2 [40]. Additionally, nodal line phonons, including unique forms such as hourglass nodal lines, nodal chains, and nodal nets, have been observed in phononic systems [41,42]. Furthermore, researchers have identified phononic systems hosting nodal surface phonons, with one, two, or three nodal surfaces in their phonon spectrum [43–45]. However, systems exclusively hosting topological charged phonons remain limited, for instance those exclusively featuring phonons characterized by different Chern numbers.

In this study, we introduce $K_2Pb_2O_3$ as a material exclusively hosting various types of phonons, including charge-1, charge-2, and charge-4 phonons (see the dispersion diagram in Fig. 1). Through a combination of symmetry analysis and

*Contact author: jinlei994@163.com
†Contact author: ying_liu@hebut.edu.cn

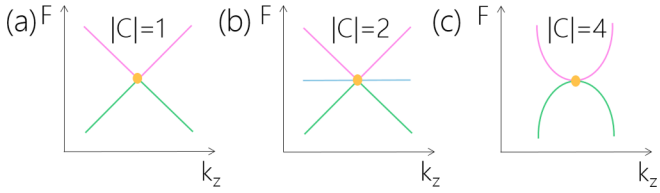

FIG. 1. Schematic diagram of phonons with nonzero topological charges mentioned in the article. (a) Weyl phonon carrying topological charge ±1, (b) TP carrying topological charge ±2, and (c) Weyl phonon carrying topological charge ±4.

first-principles calculations, we identify a Weyl phonon with a topological charge of ±4 and a triple phonon with a topological charge of ±2. These are protected by symmetry at the high symmetry points H and Γ, respectively. Additionally, a Weyl phonon with $C = \pm 1$ is observed at the high symmetry point P. To comprehensively study their topology, we not only construct an effective model describing phonons, but we also calculate their Chern number and corresponding surface states.

II. CRYSTAL STRUCTURE AND FIRST-PRINCIPLES CALCULATIONS

Bulk $K_2Pb_2O_3$ shows a body-centered-cubic structure [see Fig. 2(a)] that has been synthesized in experiments [46]. The crystals of bulk $K_2Pb_2O_3$ belong to space group no. 199. Each unit cell contains 14 atoms, including four K atoms, four Pb atoms, and six O atoms. The crystal structure has been determined, and the lattice constant is optimized as $a = b = c = 7.46$ Å. The Brillouin zone with high-symmetric points labeled is given in Fig. 2(b).

To investigate the phononic band structure, we employed the Vienna Ab initio Simulation Package (VASP), which relies on first-principles calculations within the framework of density functional theory (DFT) [47–49]. The ion potential was determined using the generalized gradient approximation

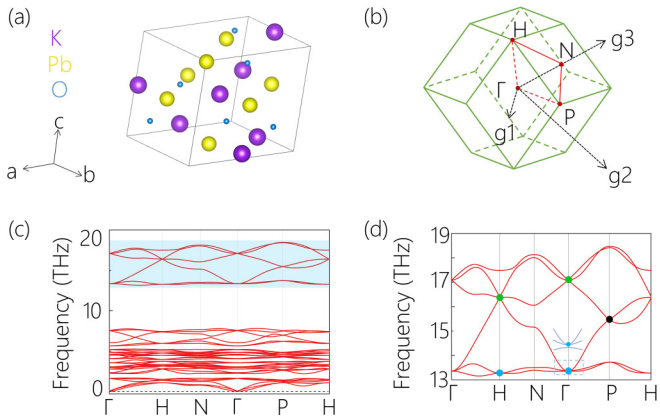

FIG. 2. (a) The primitive cell of the crystal structure for $K_2Pb_2O_3$. (b) Schematic figure for the Brillouin zone (BZ). (c) Phonon dispersion of compound $K_2Pb_2O_3$. (d) An enlarged view of the phonon dispersion in the blue box in (c). Remarkably, the inset in (d) shows that the blue dot at the high symmetry point Γ is twofold degenerate. Herein, the black, green, and blue points stand for the charge-1 WP, charge-2 TP, and charge-4 WP, respectively.

(GGA) of the Perdew-Burke-Ernzerhof (PBE) method [50]. The calculations utilized a cutoff energy of 500 eV, and for self-consistent calculation and structural optimization, a Brillouin zone (BZ) of $7 \times 7 \times 7$ with a Γ center k-point network sampling was employed. The energy convergence criterion was set to 10^{-7} eV. For the calculation of surface states, we utilized Wannier functions and the iterative Green function method implemented in the WANNIERTOOLS package [51–54].

Figure 2(c) illustrates the phononic spectrum of $K_2Pb_2O_3$. Notably, there are no imaginary frequencies observed throughout the Brillouin zone, indicating a dynamically stable structure. Specifically, in the frequency range from 13 to 19 THz, as shown in the zoomed-in image in Fig. 2(d), there are several band crossings. To elaborate, there are two triple-degenerate points marked by green dots, exhibiting linear dispersion and located at the H and Γ points, respectively. Additionally, around 13 THz, there are two doubly degenerate points (marked by blue dots) displaying quadratic dispersion. At the P point, there is also a doubly degenerate point (marked by a black dot) with linear dispersion. To study the topological properties of these band crossings in the phononic spectrum of $K_2Pb_2O_3$, we construct an effective model around these points.

III. EFFECTIVE MODELS

With respect to the triply degenerate point located at the Γ point, the little point group at this point belongs to T, which is generated by three generating operations: two twofold rotation symmetries, C_{2y} and C_{2z}, and a threefold rotation along the [111] direction, $C_{3,111}$. There exists a three-dimensional (3D) irreducible representation, Γ_4, which we select as a basis to construct the effective mode around the triple point. Notably, the time-reversal symmetry ($\mathcal{T}$) is respected in this phononic system. Under this basis, the generating operations can be written as

$$C_{3,111} = \begin{pmatrix} 0 & 0 & 1 \\ 1 & 0 & 0 \\ 0 & 1 & 0 \end{pmatrix}, \; C_{2z} = \begin{pmatrix} -1 & 0 & 0 \\ 0 & -1 & 0 \\ 0 & 0 & 1 \end{pmatrix}, \quad (1)$$

$$C_{2y} = \begin{pmatrix} -1 & 0 & 0 \\ 0 & 1 & 0 \\ 0 & 0 & -1 \end{pmatrix}, \; \mathcal{T} = \begin{pmatrix} 1 & 0 & 0 \\ 0 & 1 & 0 \\ 0 & 0 & 1 \end{pmatrix} \mathcal{K}. \quad (2)$$

Here, $\mathcal{K}$ represents the complex conjugation. Constrained by these operations, the effective model around the triple point is given by

$$\mathcal{H}_{\mathrm{TP}}(\boldsymbol{k}) = c \begin{pmatrix} 0 & ik_x & -ik_z \\ -ik_x & 0 & ik_y \\ ik_z & -ik_y & 0 \end{pmatrix}, \quad (3)$$

where c stands for a real parameter. In particular, the matrices that form the Hamiltonian are based on three matrices, with

$$S_x = \begin{pmatrix} 0 & i & 0 \\ -i & 0 & 0 \\ 0 & 0 & 0 \end{pmatrix}, \; S_y = \begin{pmatrix} 0 & 0 & 0 \\ 0 & 0 & i \\ 0 & -i & 0 \end{pmatrix},$$

$$S_z = \begin{pmatrix} 0 & 0 & -i \\ 0 & 0 & 0 \\ i & 0 & 0 \end{pmatrix}. \quad (4)$$

Notably, S_α, $(\alpha = x, y, z)$ is the spin-1 matrix, satisfying the algebra of angular momentum: $[S_\alpha, S_\beta] = i\epsilon_{\alpha\beta\gamma}S_\gamma$. The spin-1 matrix in Eq. (4) is equivalent to that expressed in the eigenspace of S_z, requiring only a unitary transformation to convert between the two forms. Consequently, the Hamiltonian could take the form

$$\mathcal{H}_{\mathrm{TP}} = c\boldsymbol{k}\cdot\boldsymbol{S}. \tag{5}$$

Hence, the triple point at the Γ point is a charge-2 triple point, corresponding to a pseudospin-1 particle.

Turning to the doubly degenerate point around 13 THz at the Γ point, the crossing bands belong to Γ_2 and Γ_3, respectively. Taking them as a basis, $\{\Gamma_2,\ \Gamma_3\}$, the generating operations can be written as

$$C_{3,111} = -\frac{1}{2}\sigma_0 + \frac{i\sqrt{3}}{2}\sigma_z,\ C_{2y} = C_{2z} = \sigma_0,\ \mathcal{T} = \sigma_x\mathcal{K}, \tag{6}$$

where σ_0 represents a 2×2 identity matrix, and σ_i $(i = x, y, z)$ stands for the Pauli matrix. Under the constraints from symmetry operations, the effective model describing this point is given by

$$\begin{aligned}\mathcal{H}_\Gamma = {} & (c_0 + c_1k^2)\sigma_0 + \sqrt{3}\left[c_2k_x^2 + c_3k_y^2 - (c_2 + c_3)k_z^2\right]\sigma_x \\ & - \left[c_3\left(2k_x^2 - k_y^2 - k_z^2\right) + c_2\left(k_x^2 + k_z^2 - 2k_y^2\right)\right]\sigma_y \\ & + c_4k_xk_yk_z\sigma_z.\end{aligned} \tag{7}$$

Here, $k^2 = k_x^2 + k_y^2 + k_z^2$. Based on Eq. (7), one could observe that the dispersion along the [111] direction is cubic. Furthermore, this model carries a charge equal to ±4.

We also note that the little point group at the H point is same as that of the Γ point. In addition, this point is also invariant under $\mathcal{T}$. Hence, the triple and double points at the H point could take the same forms as those of the Γ point. In other words, the triple point at the H point can be described by Eq. (5), carrying topological charge 2, while the emergent quasiparticle around the doubly degenerate point takes the form of Eq. (7), suggesting a charge-4 topological quasiparticle.

Distinct from the Γ and H points, the P point is not a time-reversal invariant point, and band crossings at the P point are only enforced by spatial symmetries. We have checked that the little point group at the P point also belongs to T, and there are three 2D irreducible representations corresponding to it that appear at the P point, namely P_1, P_2, P_3. We separately take them as the basis. The matrix representations of generating elements can be given as

$$\mathcal{C}_{3,111} = \Lambda(\sigma_0 - i\sigma_z - i\sigma_x + i\sigma_y),\ \mathcal{C}_{2y} = \sigma_x. \tag{8}$$

Here, $\Lambda = -1/2$, $e^{i\pi/3}$, or $e^{-i\pi/3}$ corresponding to these three irreducible representations. As a consequence, the effective model of WP at the P point of SG 199 could be written as

$$\begin{aligned}\mathcal{H}_P &= c_0\sigma_0 + c_1(q_z\sigma_z + q_x\sigma_x + q_y\sigma_y) \\ &= c_0\sigma_0 + c_1\boldsymbol{q}\cdot\boldsymbol{\sigma}\end{aligned} \tag{9}$$

under these bases. Here, $(q_x, q_y, q_z) = (k_z, -k_x, k_y)$. This is a standard model that describes a conventional Weyl point, suggesting that it carries a topological charge equal to 1. In addition, this result also implies that all of the degenerate points at the P point are conventional Weyl points, carrying a topological charge −1.

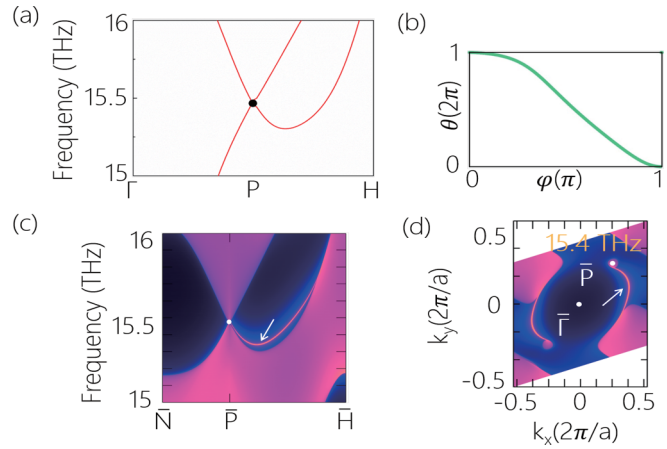

FIG. 3. (a) Enlarged phonon bands for the WP at the P point. Part (b) indicates the corresponding evolution of the sum of the Wannier charge centers (WCCs) on the sphere that encloses the charge-1 WP at the P point. The green curve indicates a WP with the Chern number $C = -1$. (c), (d) Corresponding projected surface states in the (001) surface and the constant frequency slice at 15.4 THz.

IV. TOPOLOGICAL PROPERTIES OF BAND CROSSINGS

According to symmetry analysis, we have determined that the material $K_2Pb_2O_3$ has charge-2 TP and charge-4 WP at the Γ and H points, and charge-1 WP at the P point. Next, we concretely discuss the topological properties of band crossings based on first-principles calculations.

First, let us discuss the charge-1 WP at the high symmetry point P. The phonon spectrum in Fig. 3(a) clearly shows that there is a twofold-degenerate point (marked by a black dot) at the P point, located at around 15.5 THz. To study the topology for this point, we perform the Wilson loop method to calculate its Chern number. As shown in Fig. 3(b), the result indicates that such a WP is characterized by a nonzero Chern number, equal to −1. The Fermi arc is one of the typical characteristics of the WP. We perform a projection onto the (001) plane to study its surface states, as shown in Fig. 3(c), and the corresponding constant frequency slice at 15.4 THz is shown in Fig. 3(d). As expected, one Fermi arc steam from the projection of WP.

Now we will address the charge-2 TP at high-symmetry points Γ and H. The corresponding enlarged phonon spectrum along the N-Γ-P path is shown in Fig. 4(a). For TP, it can be described by the Hamiltonian $c\boldsymbol{k}\cdot S$. Notably, S_α $(\alpha = x, y, z)$ is the spin-1 matrix satisfying the algebra of angular momentum: $[S_\alpha, S_\beta] = i\epsilon_{\alpha\beta\gamma}S_\gamma$. The Wilson loops given in Fig. 4(b) demonstrate that the Chern number of TP at the Γ point is −2. The schematic diagram of the charge-2 TP is shown in Fig. 1(b). According to the bulk-surface correspondence, the nonzero Chern number gives rise to two Fermi arcs. We plot the surface spectra on the (001) surface. The result is shown in Fig. 4(c), with two Fermi arcs along the $\bar{H}$-$\bar{\Gamma}$-$\bar{P}$ path denoted by white arrows. Correspondingly, we also plot the constant frequency slice at 17.1 THz in Fig. 4(d), and we can still

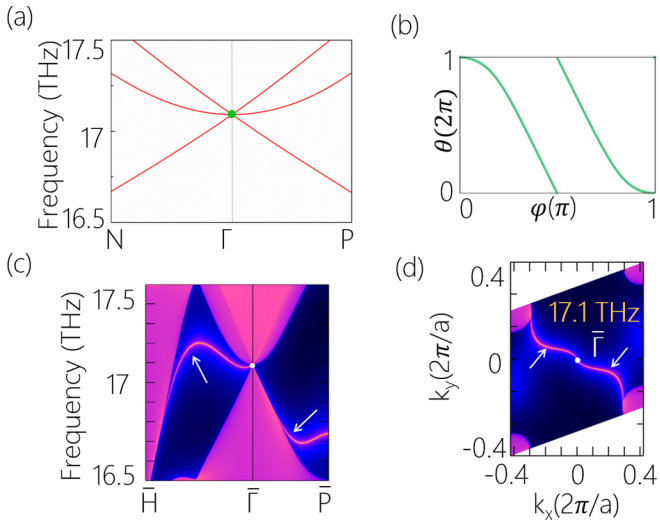

FIG. 4. (a) Enlarged phonon bands for the TP at the Γ point. (b) The evolutions of the sum of WCCs on the spheres that enclose the charge-2 TP at the Γ point. The green curve indicates a TP with the Chern number $C = -2$. (c), (d) Corresponding projected surface states in the (001) surface and the constant frequency slice at 17.1 THz.

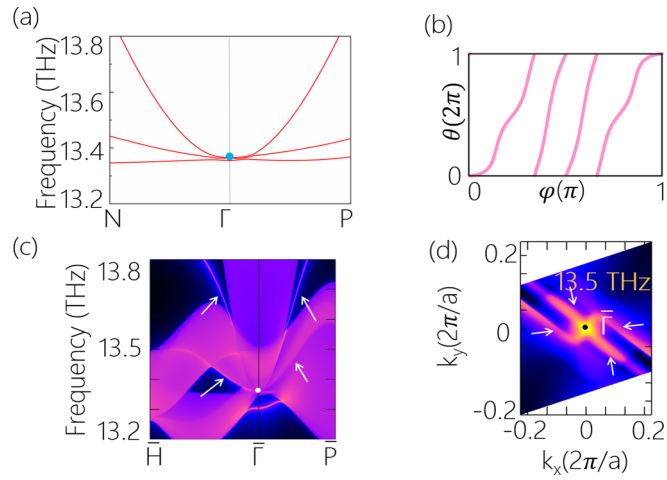

FIG. 6. (a) Enlarged phonon bands for the WP at the Γ point. (b) The evolutions of the sum of WCCs on the spheres that enclose the charge-4 WP at the Γ point. The pink curve indicates a WP with the Chern number $C = +4$. (c), (d) Corresponding projected surface states in the (001) surface and the constant frequency slice at 13.5 THz.

observe two Fermi arcs from the $\bar{\Gamma}$ point. Similarly, for TP at the H point, we also plot the Wilson loop in Fig. 5(b), which indicates that there is a nonzero Chern number equal to $+2$. We can also observe two clear Fermi arcs emanating from the projection of TP at the H point, as shown in Figs. 5(c) and 5(d). By the way, the TP in electronic systems is discussed systematically in our previous work [27].

Next, we discuss the charge-4 WP at the high symmetry points Γ and H. For the WP with $C = \pm 4$ in the electronic system, Zhang *et al*. have predicted that LaIrSi-type materials (SG 199) can carry $C = \pm 4$ WP at the high symmetry point without considering the spin-orbit coupling effect [21]. Here, we find the charge-4 WP in a phononic system. Figure 6(a) shows the corresponding phonon spectrum around the charge-4 WP at the Γ point. Using the Wilson loop method, we calculate the Chern number for the WP, as shown in Fig. 6(b). The result indicates the WP with the Chern number $C = +4$. When projected onto the (001) plane, as shown in Fig. 6(c), there are four Fermi arcs emanating from its projection. In its corresponding phonon constant frequency slice at 13.5 THz,

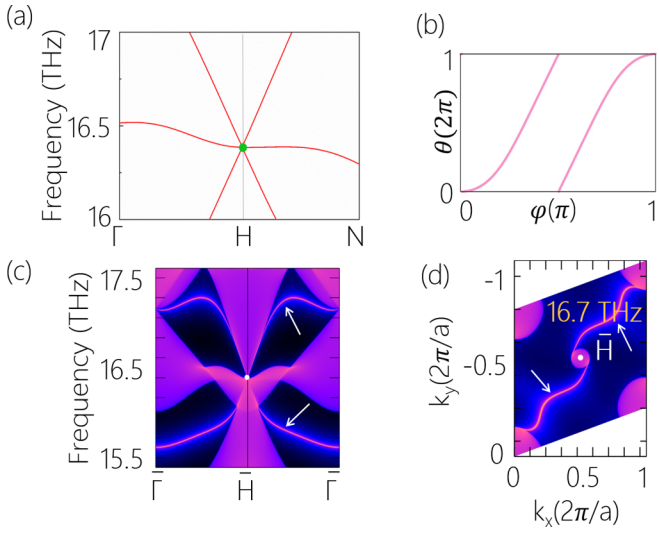

FIG. 5. (a) Enlarged phonon bands for the TP at the H point. (b) The evolutions of the sum of the WCCs on the spheres that enclose the charge-2 TP at the H point. The pink curve indicates a TP with a Chern number $C = +2$. (c), (d) Corresponding projected surface states in the (001) surface and the constant frequency slice at 16.7 THz.

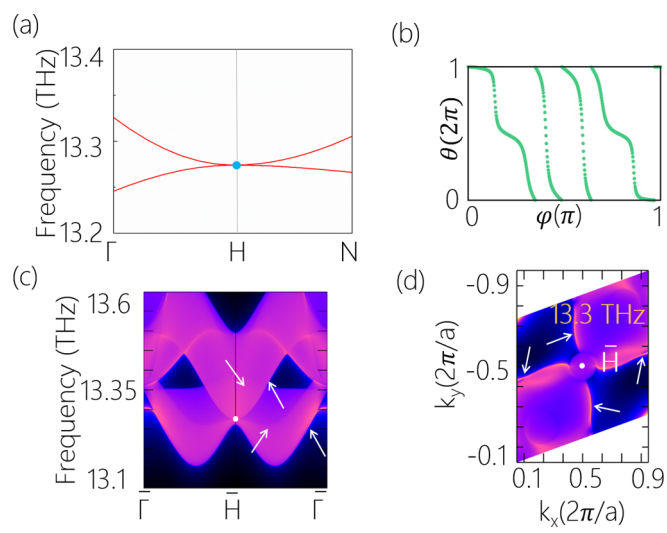

FIG. 7. (a) Enlarged phonon bands for the WP at the H point. (b) The evolutions of the sum of WCCs on the spheres that enclose the charge-4 WP at the H point. The green curve indicates a WP with the Chern number $C = -4$. (c), (d) Corresponding projected surface states in the (001) surface and the constant frequency slice at 13.3 THz.

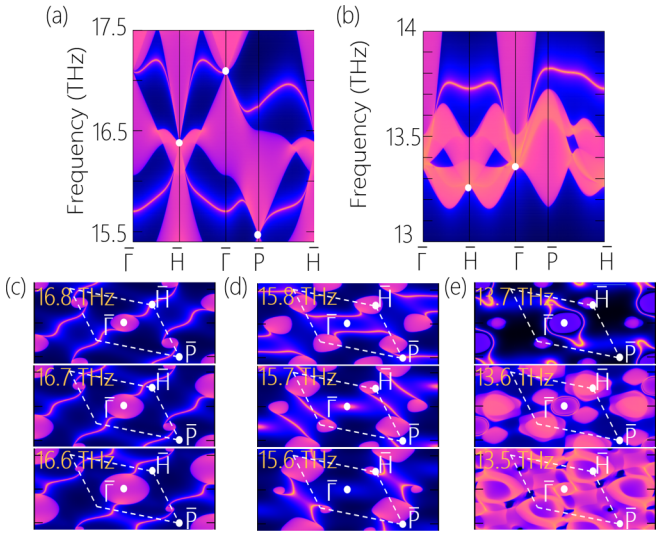

FIG. 8. (a), (b) The surface state projection on the (001) surface for $K_2Pb_2O_3$ along the Γ-H-Γ-P-H surface paths with a frequency of 15.5–17.5 THz and 13–14 THz, respectively. (c)–(e) Isofrequency surface contours of the (001) surface at frequencies of 16.6, 16.7, 16.8, 15.6, 15.7, 15.8, 13.5, 13.6, and 13.7 THz, respectively. Remarkably, the white dotted boxes in (c)–(e) represent the BZ projection to the (001) direction.

we also clearly observe four Fermi arcs, as shown in Fig. 6(d). Similarly, the charge-4 WP at the H point has the same result as that at the Γ point. It carries a nonzero topological charge, equal to −4, demonstrated by the Wilson loops in Fig. 7(b). The surface state projected onto the (001) surface is shown in Fig. 7(c). There are four Fermi arcs denoted by white arrows. In the constant frequency slice at 13.3 THz, we can also observe Fermi arcs in Fig. 7(d).

Finally, in order to clarify the relationship between the charge-1 WP, charge-2 TP, and charge-4 WP, we plot the surface states along the $\bar{\Gamma}$-$\bar{H}$-$\bar{\Gamma}$-$\bar{P}$-$\bar{H}$ path in the frequency ranges of 15.5–17.5 THz and 13–14 THz, as shown in Figs. 8(a) and 8(b), respectively. The result shows that two Fermi arcs emanating from the charge-1 WP, charge-2 TP, and charge-4 WP are connected to each other, forming a long Fermi arc extended in the whole BZ. To further observe the evolution of the surface states at different frequency, we also calculate a series of constant frequency slices in Figs. 8(c)–8(e).

V. DISCUSSION AND CONCLUSION

Before closing, we would like to make several remarks. $K_2Pb_2O_3$ is an ideal topological phononic system that has the following characteristics: (i) In the range of 13–19 THz, multiple phonons with nonzero topological charges (charge-4 WP, charge-2 TP, and charge-1 WP) coexist. (ii) All phonon excitations are robust due to the protection of symmetry. (iii) The material shows clear surface states, and the Fermi arcs emanating from the projections of charge-1 WP, charge-2 TP, and charge-4 WP are connected to each other, forming a long Fermi arc extended in the whole Brillouin zone. Such a long Fermi arc greatly facilitates the observation of nontrivial phonon surface states in experiment by neutron scatterings or high-resolution electron energy loss spectroscopy. Moreover, the novel physical properties related to the Fermi arcs and further applications are also expected to be observed and realized. (iv) The WP and TP phonons in $K_2Pb_2O_3$ all have Chern numbers greater than zero, and they are expected to exhibit particular phonon-based transport behaviors and enhanced thermoelectric response [36,55,56]. This is similar to charged topological fermions, which can realize negative magnetoresistance, the quantized circular photogalvanic effect, and so on [24,57–60].

In conclusion, we propose a realistic material $K_2Pb_2O_3$ that simultaneously hosts charge-4 WPs, charge-2 TPs, and charge-1 WPs. These topological phonons are studied comprehensively by combining symmetry analysis and first-principles calculations. We give the symmetry conditions of realizing these topological phonons, and we construct the effective model to describe them. We reveal that the material has WPs and TPs at the H, Γ, and P points in the range 13–19 THz. These points all have a nonzero Chern number. Their Fermi arcs are very clear and connected to each other, extended in the whole BZ, which is promising to be observed in experiment. Our results provide an ideal material for exploring the excitation of phonons carrying nonzero topological charges.

ACKNOWLEDGMENTS

This work is supported by the Hebei Natural Science Foundation (No. A2023202009 and No. A2023202032), the Postdoctoral Fellowship Program of CPSF (No. GZC20230662), and the Overseas Scientists Sponsorship Program of Hebei Province (No. C20230320).

[1] A. H. Castro Neto, F. Guinea, N. M. R. Peres, K. S. Novoselov, and A. K. Geim, The electronic properties of graphene, Rev. Mod. Phys. **81**, 109 (2009).

[2] X. Wan, A. M. Turner, A. Vishwanath, and S. Y. Savrasov, Topological semimetal and Fermi-arc surface states in the electronic structure of pyrochlore iridates, Phys. Rev. B **83**, 205101 (2011).

[3] Y. Ando, Topological insulator materials, J. Phys. Soc. Jpn. **82**, 102001 (2013).

[4] Z. Liu, B. Zhou, Y. Zhang, Z. Wang, H. Weng, D. Prabhakaran, S.-K. Mo, Z. Shen, Z. Fang, X. Dai *et al.*, Discovery of a three-dimensional topological Dirac semimetal, Na_3Bi, Science **343**, 864 (2014).

[5] S.-Y. Xu, I. Belopolski, N. Alidoust, M. Neupane, G. Bian, C. Zhang, R. Sankar, G. Chang, Z. Yuan, C.-C. Lee *et al.*, Discovery of a Weyl fermion semimetal and topological Fermi arcs, Science **349**, 613 (2015).

[6] Y. Liu, Z.-M. Yu, C. Xiao, and S. A. Yang, Quantized circulation of anomalous shift in interface reflection, Phys. Rev. Lett. **125**, 076801 (2020).

[7] M.-X. Wang, C. Liu, J.-P. Xu, F. Yang, L. Miao, M.-Y. Yao, C. Gao, C. Shen, X. Ma, X. Chen *et al.*, The coexistence of

superconductivity and topological order in the Bi_2Se_3 thin films, Science **336**, 52 (2012).

[8] J. Wang, Q. Zhou, B. Lian, and S.-C. Zhang, Chiral topological superconductor and half-integer conductance plateau from quantum anomalous Hall plateau transition, Phys. Rev. B **92**, 064520 (2015).

[9] Z. Wang, Y. Sun, X.-Q. Chen, C. Franchini, G. Xu, H. Weng, X. Dai, and Z. Fang, Dirac semimetal and topological phase transitions in A_3Bi (A = Na, K, Rb), Phys. Rev. B **85**, 195320 (2012).

[10] S.-Y. Xu, C. Liu, S. K. Kushwaha, R. Sankar, J. W. Krizan, I. Belopolski, M. Neupane, G. Bian, N. Alidoust, T.-R. Chang *et al.*, Observation of Fermi arc surface states in a topological metal, Science **347**, 294 (2015).

[11] Y. Xu, F. Zhang, and C. Zhang, Structured Weyl points in spin-orbit coupled fermionic superfluids, Phys. Rev. Lett. **115**, 265304 (2015).

[12] Y. Sun, S.-C. Wu, M. N. Ali, C. Felser, and B. Yan, Prediction of Weyl semimetal in orthorhombic $MoTe_2$, Phys. Rev. B **92**, 161107(R) (2015).

[13] N. Kumar, Y. Sun, M. Nicklas, S. J. Watzman, O. Young, I. Leermakers, J. Hornung, J. Klotz, J. Gooth, K. Manna *et al.*, Extremely high conductivity observed in the triple point topological metal MoP, Nat. Commun. **10**, 2475 (2019).

[14] N. Kumar, M. Yao, J. Nayak, M. G. Vergniory, J. Bannies, Z. Wang, N. B. Schröter, V. N. Strocov, L. Müchler, W. Shi *et al.*, Signatures of sixfold degenerate exotic fermions in a superconducting metal $PdSb_2$, Adv. Mater. **32**, 1906046 (2020).

[15] R. Chapai, A. Rydh, M. P. Smylie, D. Y. Chung, H. Zheng, A. E. Koshelev, J. E. Pearson, W.-K. Kwok, J. F. Mitchell, and U. Welp, Superconducting properties of the spin Hall candidate Ta_3Sb with eightfold degeneracy, Phys. Rev. B **105**, 184510 (2022).

[16] L. Jin, X. Zhang, Y. Liu, X. Dai, X. Shen, L. Wang, and G. Liu, Two-dimensional Weyl nodal-line semimetal in a d^0 ferromagnetic K_2N monolayer with a high Curie temperature, Phys. Rev. B **102**, 125118 (2020).

[17] X. Zhang, L. Jin, X. Dai, G. Chen, and G. Liu, Ideal inner nodal chain semimetals in Li_2XY (X = Ca, Ba; Y= Si, Ge) materials, J. Phys. Chem. Lett. **9**, 5358 (2018).

[18] L. Wang, L. Jin, G. Liu, Y. Liu, X. Dai, and X. Zhang, Theoretical realization of two-dimensional Dirac/Weyl line-node and traversing edge states in penta-X_2Y monolayers, Appl. Mater. Today **23**, 101057 (2021).

[19] C. Fang, M. J. Gilbert, X. Dai, and B. A. Bernevig, Multi-Weyl topological semimetals stabilized by point group symmetry, Phys. Rev. Lett. **108**, 266802 (2012).

[20] S. S. Tsirkin, I. Souza, and D. Vanderbilt, Composite Weyl nodes stabilized by screw symmetry with and without time-reversal invariance, Phys. Rev. B **96**, 045102 (2017).

[21] T. Zhang, R. Takahashi, C. Fang, and S. Murakami, Twofold quadruple Weyl nodes in chiral cubic crystals, Phys. Rev. B **102**, 125148 (2020).

[22] A. A. Burkov, M. D. Hook, and L. Balents, Topological nodal semimetals, Phys. Rev. B **84**, 235126 (2011).

[23] Z. Ni, K. Wang, Y. Zhang, O. Pozo, B. Xu, X. Han, K. Manna, J. Paglione, C. Felser, A. G. Grushin *et al.*, Giant topological longitudinal circular photo-galvanic effect in the chiral multifold semimetal CoSi, Nat. Commun. **12**, 154 (2021).

[24] F. De Juan, A. G. Grushin, T. Morimoto, and J. E. Moore, Quantized circular photogalvanic effect in Weyl semimetals, Nat. Commun. **8**, 15995 (2017).

[25] F. Flicker, F. de Juan, B. Bradlyn, T. Morimoto, M. G. Vergniory, and A. G. Grushin, Chiral optical response of multifold fermions, Phys. Rev. B **98**, 155145 (2018).

[26] F. de Juan, Y. Zhang, T. Morimoto, Y. Sun, J. E. Moore, and A. G. Grushin, Difference frequency generation in topological semimetals, Phys. Rev. Res. **2**, 012017(R) (2020).

[27] L. Tian, Y. Liu, W.-W. Yu, X. Zhang, and G. Liu, Triple degenerate point in three dimensions: Theory and realization, Phys. Rev. B **104**, 045137 (2021).

[28] W.-W. Yu, Y. Liu, W. Meng, H. Liu, J. Gao, X. Zhang, and G. Liu, Phononic higher-order nodal point in two dimensions, Phys. Rev. B **105**, 035429 (2022).

[29] C. Wang, W.-W. Yu, Y. Liu, X. Zhang, L. Jin, C. Liu, and G. Liu, Two-dimensional Dirac phonons without/with inversion symmetry, J. Phys.: Condens. Matter **35**, 425702 (2023).

[30] X. Wang, T. Yang, Z. Cheng, G. Surucu, J. Wang, F. Zhou, Z. Zhang, and G. Zhang, Topological nodal line phonons: Recent advances in materials realization, Appl. Phys. Rev. **9**, 041304 (2022).

[31] M. Xiao, L. Ye, C. Qiu, H. He, Z. Liu, and S. Fan, Experimental demonstration of acoustic semimetal with topologically charged nodal surface, Sci. Adv. **6**, eaav2360 (2020).

[32] R. Wang, B. W. Xia, Z. J. Chen, B. B. Zheng, Y. J. Zhao, and H. Xu, Symmetry-protected topological triangular Weyl complex, Phys. Rev. Lett. **124**, 105303 (2020).

[33] T. Zhang, Z. Song, A. Alexandradinata, H. Weng, C. Fang, L. Lu, and Z. Fang, Double-Weyl phonons in transition-metal monosilicides, Phys. Rev. Lett. **120**, 016401 (2018).

[34] H.-H. Fu, Q.-B. Liu, Z.-Q. Wang, and X.-F. Yang, Multi-fold fan-shape surface state induced by an isolated Weyl phonon beyond no-go theorem, Adv. Sci. **10**, 2207508 (2023).

[35] H. Miao, T. T. Zhang, L. Wang, D. Meyers, A. H. Said, Y. L. Wang, Y. G. Shi, H. M. Weng, Z. Fang, and M. P. M. Dean, Observation of double Weyl phonons in parity-breaking FeSi, Phys. Rev. Lett. **121**, 035302 (2018).

[36] S. Singh, Q. S. Wu, C. Yue, A. H. Romero, and A. A. Soluyanov, Topological phonons and thermoelectricity in triple-point metals, Phys. Rev. Mater. **2**, 114204 (2018).

[37] Y. Yang, Cubic Ca_3I_3P with ideal charge-two triple point, Front. Phys. **10**, 1058242 (2022).

[38] T. Yang, C. Xie, H. Chen, X. Wang, and G. Zhang, Phononic nodal points with quadratic dispersion and multifold degeneracy in the cubic compound Ta_3Sn, Phys. Rev. B **105**, 094310 (2022).

[39] Y. Yang, J. Wang, Y. Liu, Y. Cui, G. Ding, and X. Wang, Topological phonons in Cs-Te binary systems, Phys. Rev. B **107**, 024304 (2023).

[40] W.-W. Yu, Y. Liu, X. Zhang, and G. Liu, Topological charge-2 Dirac phonons in three dimensions: Theory and realization, Phys. Rev. B **106**, 195142 (2022).

[41] W.-W. Yu, C. Wang, X. Zhang, G. Liu, J. Wang, Z. Wu, and Y. Liu, Hourglass nodal loop phonons in two dimensions jointly supported by fourfold rotation and glide mirror symmetries, Phys. Rev. B **108**, 045139 (2023).

[42] G. Ding, T. Sun, and X. Wang, Ideal nodal-net, nodal-chain, and nodal-cage phonons in some realistic materials, Phys. Chem. Chem. Phys. **24**, 11175 (2022).

[43] Q.-B. Liu, Z.-Q. Wang, and H.-H. Fu, Ideal topological nodal-surface phonons in RbTeAu-family materials, Phys. Rev. B **104**, L041405 (2021).

[44] C. Xie, H. Yuan, Y. Liu, and X. Wang, Two-nodal surface phonons in solid-state materials, Phys. Rev. B **105**, 054307 (2022).

[45] C. Xie, H. Yuan, Y. Liu, X. Wang, and G. Zhang, Three-nodal surface phonons in solid-state materials: Theory and material realization, Phys. Rev. B **104**, 134303 (2021).

[46] K.-P. Martens and R. Hoppe, Zum System K_2O/PbO. Zur Kenntnis von $K_2Pb_2O_3$, Z. Anorg. Allg. Chem. **437**, 116 (1977).

[47] G. Kresse and J. Hafner, Ab initio molecular-dynamics simulation of the liquid-metal–amorphous-semiconductor transition in germanium, Phys. Rev. B **49**, 14251 (1994).

[48] G. Kresse and J. Furthmüller, Efficient iterative schemes for ab initio total-energy calculations using a plane-wave basis set, Phys. Rev. B **54**, 11169 (1996).

[49] P. E. Blöchl, Projector augmented-wave method, Phys. Rev. B **50**, 17953 (1994).

[50] J. P. Perdew, K. Burke, and M. Ernzerhof, Generalized gradient approximation made simple, Phys. Rev. Lett. **77**, 3865 (1996).

[51] N. Marzari and D. Vanderbilt, Maximally localized generalized Wannier functions for composite energy bands, Phys. Rev. B **56**, 12847 (1997).

[52] I. Souza, N. Marzari, and D. Vanderbilt, Maximally localized Wannier functions for entangled energy bands, Phys. Rev. B **65**, 035109 (2001).

[53] M. L. Sancho, J. L. Sancho, J. L. Sancho, and J. Rubio, Highly convergent schemes for the calculation of bulk and surface Green functions, J. Phys. F **15**, 851 (1985).

[54] Q. Wu, S. Zhang, H.-F. Song, M. Troyer, and A. A. Soluyanov, WannierTools: An open-source software package for novel topological materials, Comput. Phys. Commun. **224**, 405 (2018).

[55] D.-S. Tang and B.-Y. Cao, Topological effects of phonons in GaN and AlGaN: A potential perspective for tuning phonon transport, J. Appl. Phys. **129**, 085102 (2021).

[56] X. Jin, D.-s. Ma, P. Yu, X. Ding, R. Wang, X. Lv, and X. Yang, Strain-driven phonon topological phase transition impedes thermal transport in titanium monoxide, Cell Rep. Phys. Sci. **5**, 101895 (2024).

[57] D. T. Son and B. Z. Spivak, Chiral anomaly and classical negative magnetoresistance of Weyl metals, Phys. Rev. B **88**, 104412 (2013).

[58] J. Cano, B. Bradlyn, Z. Wang, M. Hirschberger, N. P. Ong, and B. A. Bernevig, Chiral anomaly factory: Creating Weyl fermions with a magnetic field, Phys. Rev. B **95**, 161306(R) (2017).

[59] E. J. König, H.-Y. Xie, D. A. Pesin, and A. Levchenko, Photogalvanic effect in Weyl semimetals, Phys. Rev. B **96**, 075123 (2017).

[60] Z. Ji, G. Liu, Z. Addison, W. Liu, P. Yu, H. Gao, Z. Liu, A. M. Rappe, C. L. Kane, E. J. Mele *et al.*, Spatially dispersive circular photogalvanic effect in a Weyl semimetal, Nat. Mater. **18**, 955 (2019).